PROTOLITH AFFILIATION AND TECTONOMETAMORPHIC EVOLUTION OF THE GURLA MANDHATA CORE COMPLEX, NW NEPAL HIMALAYA

LAURENT GODIN[1†], MARK AHENDA[1], DJORDJE GRUJIC[2], ROSS STEVENSON[3], AND JOHN COTTLE[4]

[1] *Geological Sciences and Geological Engineering, Queen´s University, Kingston, Ontario, Canada, K7L 3N6*
[2] *Department of Earth and Environmental Sciences, Dalhousie University, 1459 Oxford Street, Halifax, NS B3H 4R2, Canada*
[3] *GÉOTOP and Département des Sciences de la Terre et de l'Atmosphère - Université du Québec à Montréal, C.P. 8888, Succursale Centre-Ville, Montréal, QC, Canada H3C 3P8*
[4] *Department of Earth Science, University of California, Santa Barbara, CA 93106-9630, USA*

SUPPLEMENTARY FILE 1

1A. Sm-Nd analytical procedures

Rock samples were crushed and pulverized using a ceramic mortar and pestle, then dissolved using lithium borate fusion and analyzed on ICP-ES for major elements and ICP-MS for Rare Earth Elements (REEs) and other trace elements.

Sm-Nd isotopic analyses were performed at GÉOTOP – Université du Québec à Montréal. 80-110 mg of powder of each sample was spiked with a $^{150}Nd/^{149}Sm$-enriched spike and dissolved in a mixture of 15N HNO3 and 29N HF over 5-7 days. The resulting fluoride salts were treated with 16N HNO3 and 6N HCl to dissolve and enhance the solubility of the REEs. Iron was removed by loading samples in ion-exchange polyprep columns with AG1X8 resin and 6N HCl. The REEs were isolated with TRU Spec resin using 0.05N HNO3, and Nd and Sm were separated with LN Spec resin using 0.2N, 0.3N, and 0.5N HCl. The Nd and Sm fractions were loaded onto Re filaments and analyzed on a TRITON PLUS thermal ionization mass spectrometer (TIMS) in static mode. Mass fractionation was corrected using the ratio $^{146}Nd/^{144}Nd = 0.7129$ assuming exponential fractionation behavior. The Nd isotopic compositions are expressed as $\varepsilon Nd_{(0)}$ and calculated using the present day chondritic uniform reservoir (CHUR) values of $^{143}Nd/^{144}Nd = 0.512639$ and $^{147}Sm/^{144}Nd = 0.1966$ (Goldstein et al., 1984). The $^{147}Sm/^{144}Nd$ ratios are accurate to 0.5%, corresponding to an average $\varepsilon Nd(0)$ error of ±0.5 epsilon units, based on measurements of the JNdi Nd standard ($^{143}Nd/^{144}Nd = 0.512095 \pm 5$, n=3).

1B. U-Th/Pb petrochronology and analytical procedures

Petrochronology is the interpretation of isotopic dates in light of complementary elemental or isotopic information from the same mineral(s) (Kylander-Clark et al., 2013). Yttrium (Y) zonation is a key component of monazite petrochronological interpretation. Y is

46 readily incorporated in the crystal lattice of monazite (Pyle et al., 2001). In metapelitic rocks,
47 however, garnet preferentially incorporates Y and heavy rare earth elements (HREEs) during
48 growth, depleting the free Y and HREE content of the system and leaving monazites that grew in
49 the presence of garnet Y-poor (Spear and Pyle, 2002; Pyle and Spear, 2003; Kohn et al., 2005).
50 Garnet breakdown during anatexis or decompression can release Y into the system, causing any
51 concurrently crystallizing monazite to be higher in Y content (Pyle, et al., 2001). Monazite
52 results in garnet-bearing rocks can be linked to stages of garnet growth and breakdown, and
53 therefore to prograde or retrograde metamorphism. In melt-present systems, monazite can
54 dissolve on the prograde path during partial melting but tends to recrystallize on the retrograde
55 path, still resulting in higher Y and HREE content in retrograde monazites (Kelsey et al., 2008).
56 Monazite grains were identified in thin section and selected using a Mineral Liberation
57 Analysis 650 field emission gun environmental scanning electron microscope at Queen's Facility
58 for Isotope Research (Queen's University, Kingston, Ontario, Canada). Selected grains were
59 chemically mapped for U, Th, Y, Ca, and Si with X-ray wavelength dispersive spectrometry on a
60 JEOL JXA-8230 electron microprobe, also at Queen's Facility for Isotope Research. The
61 electron microprobe experimental conditions were set at an acceleration voltage of 15 kV, beam
62 current of 200 nA, dwell time of 100 ms and step size of 0.5-1.4 μm. X-ray element maps
63 identified chemical zonation and informed laser spot locations.
64 Monazite was analyzed directly in thin section using the Laser Ablation Split Stream
65 (LASS) method at the University of California Santa Barbara. Spot location was guided with the
66 aid of X-ray compositional maps. Instrumentation consists of a Photon Machines 193 nm ArF
67 Excimer laser and 'HelEx' ablation cell coupled to a Nu Instruments HR Plasma high-resolution
68 multi-collector MC-ICP-MS (U, Th, and Pb isotopes) and an Agilent 7700S Quadrupole ICP-MS

(major and trace elements). Methods in this study follow those outlined in Kylander-Clark et al. (2013) with modifications outlined in McKinney et al. (2015). Monazite was ablated using a 7 μm diameter spot at 3 Hz repetition rate for 90 shots at a laser fluence of 1.5 J/cm2, resulting in craters that are ~4 μm deep.

Data reduction, including corrections for baseline, instrumental drift, mass bias, down-hole fractionation as well as age calculations were carried out using Iolite v. 2.5 (Paton et al. 2010). Background intensities and changes in instrumental bias were interpolated using a smoothed cubic spline while down-hole inter-element fractionation was modeled using an exponential function. Statistics for baselines, on peak intensities and isotopic ratios were calculated using the mean with a 2.S.D. outlier rejection. The ^{238}U and ^{235}U decay constants of Jaffey et al. (1971) and the ^{232}Th decay constant of Amelin and Zaitsev (2002) were employed to calculate ages. All uncertainties are quoted at 2σ and include contributions from the external reproducibility of the primary reference material for the $^{206}Pb/^{238}U$ ratios and $^{208}Pb/^{232}Th$ ratios.

Monazite U-Th/Pb data was normalized to '44069' (424 Ma $^{207}Pb/^{235}U$ ID-TIMS age, Aleinikoff et al. 2006), employed to monitor and correct for mass bias as well as Pb/U and Pb/Th down-hole fractionation. To monitor data accuracy, a reference monazite 'FC-1' (55.7 Ma $^{206}Pb/^{238}U$ ID-TIMS age, Horstwood et al. 2003) was analyzed concurrently (once every ~7 unknowns) and mass bias- and fractionation-corrected based on measured isotopic ratios of the primary reference material. During the analytical period, 21 analyses of FC-1 gave a weighted mean $^{206}Pb/^{238}U$ date of 56.0 ± 1.0 Ma, and a weighted mean $^{208}Pb/^{232}Th$ date of 55.2 ± 0.9 Ma.

Trace element data were normalized to 'Bananeira' monazite using P as an internal standard and the concentration values reported in Kylander-Clark et al., (2013). Si, Ca, and Mg levels were monitored for evidence of inclusions and ablation sites visually inspected to ensure

92 no contamination occurred during analysis. Based on the long-term reproducibility of multiple
93 secondary reference minerals, trace element concentrations are accurate to better than 5% (2σ).
94
95

1C. Supplementary back-scattered electron imagery and X-ray ion microprobe chemical maps

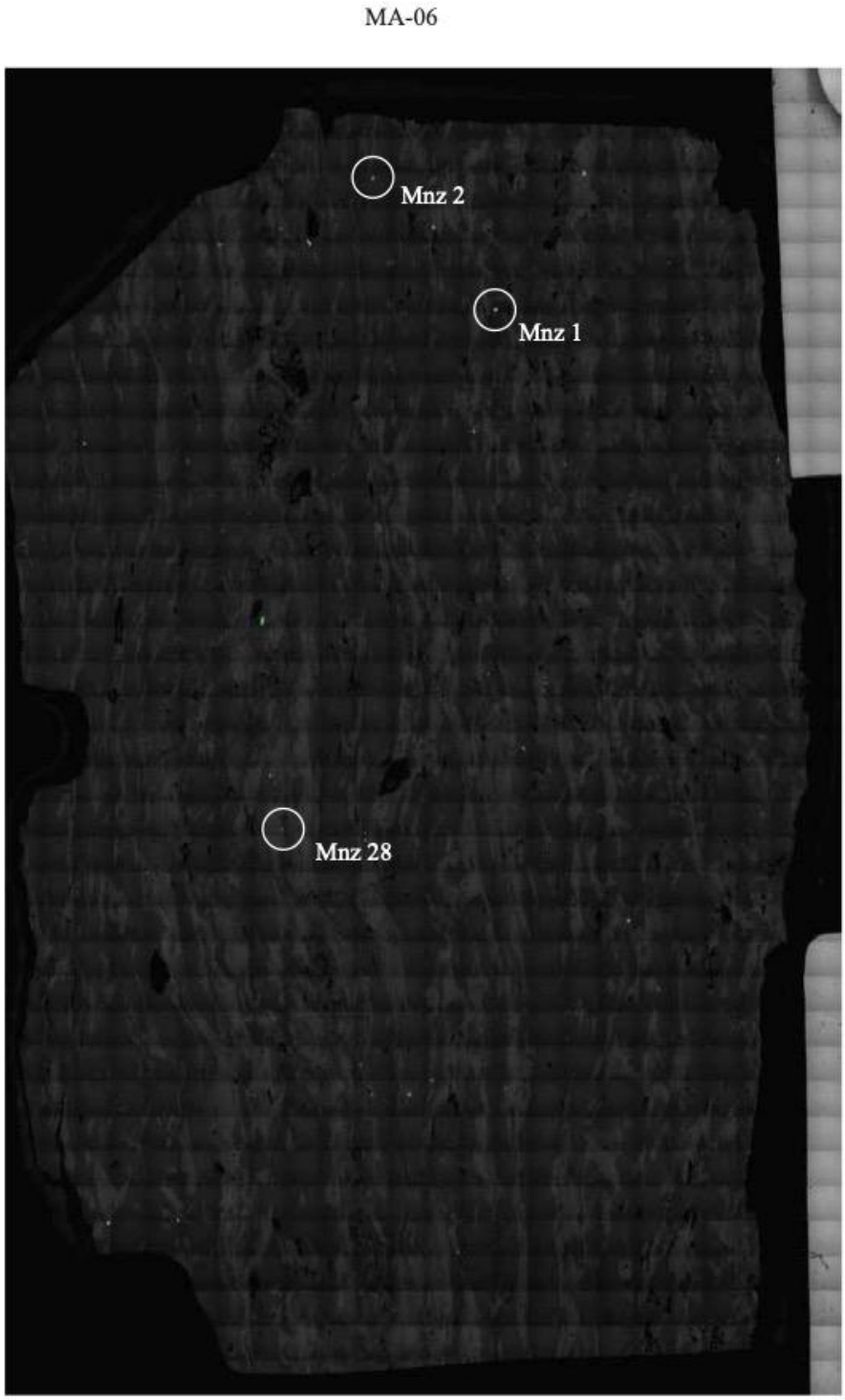

MA-06 mnz 1

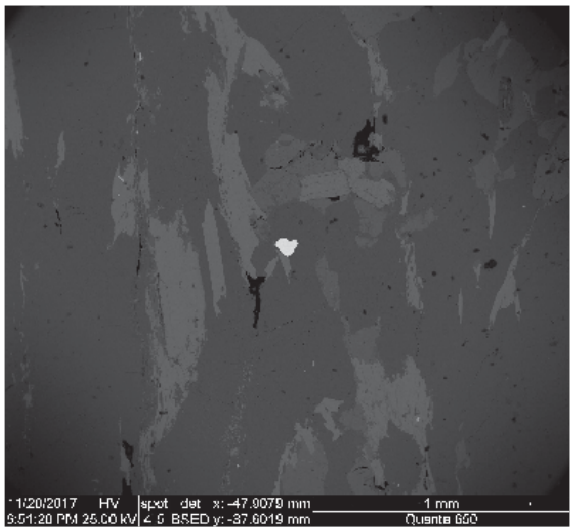

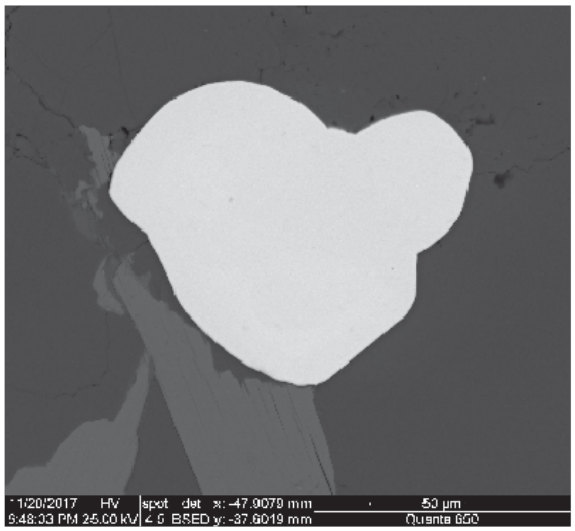

Y

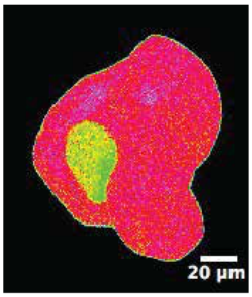

U

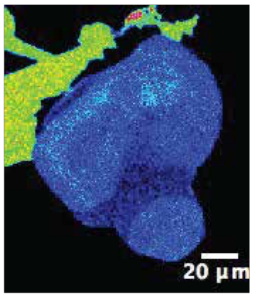

Th

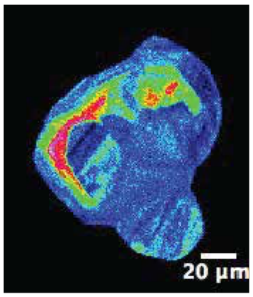

Si

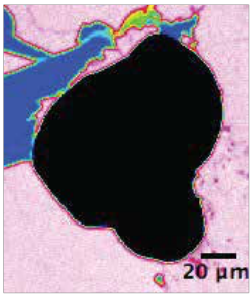

Ca

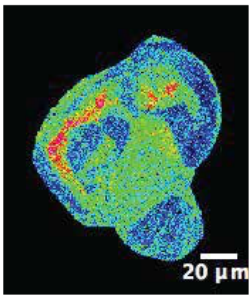

SL

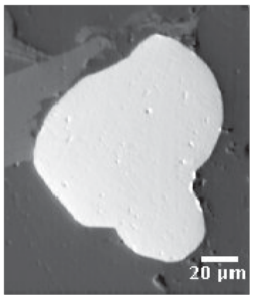

BSE

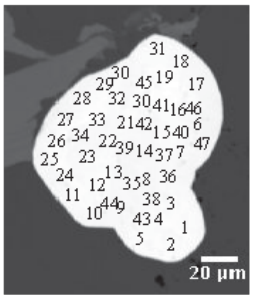

99
100
101

MA-06 mnz 2

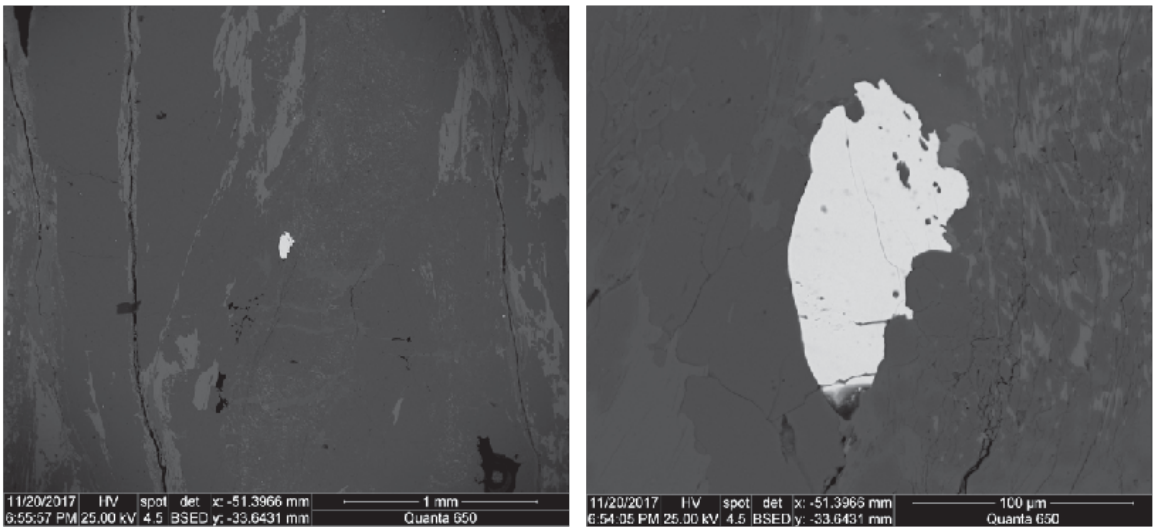

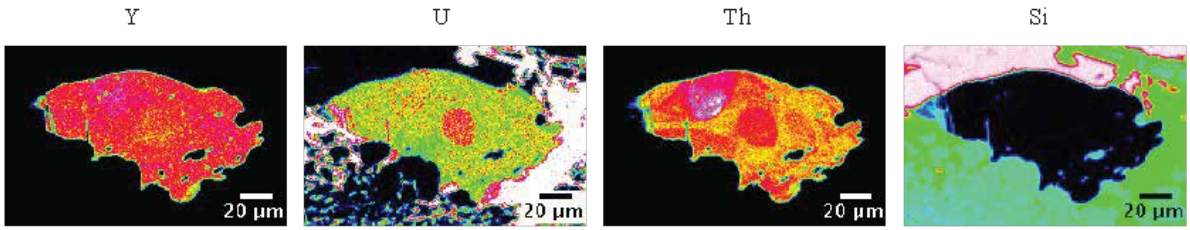

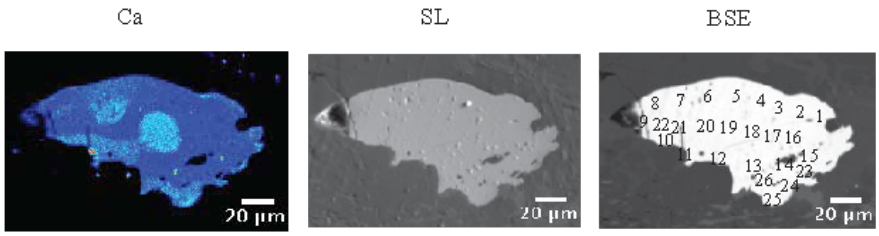

102
103
104

MA-06 mnz 28

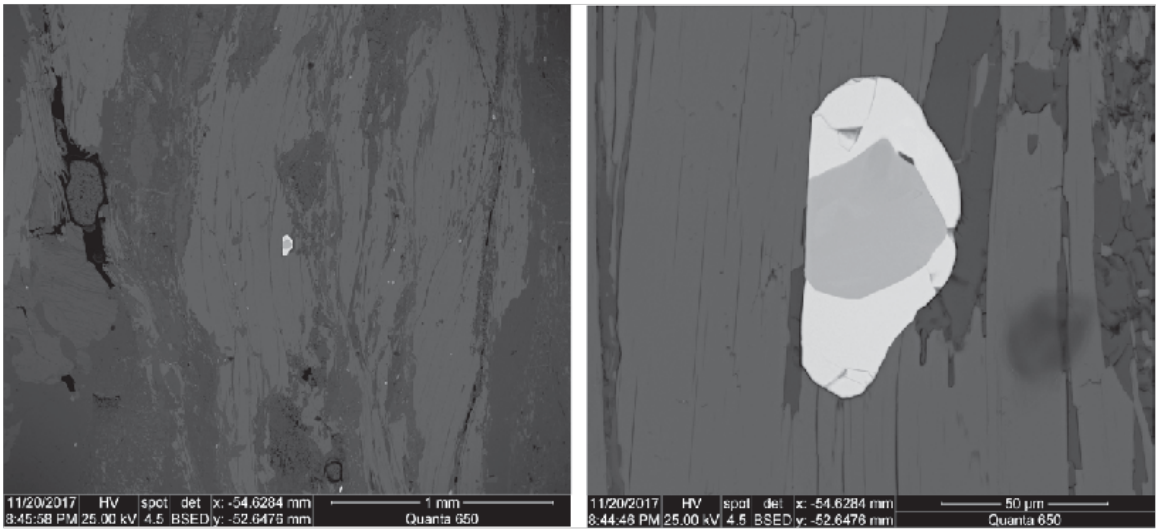

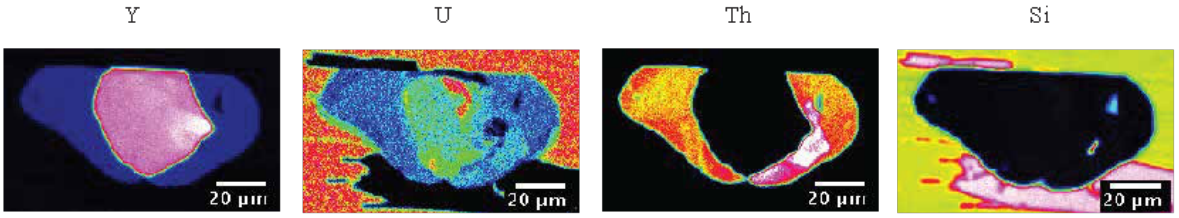

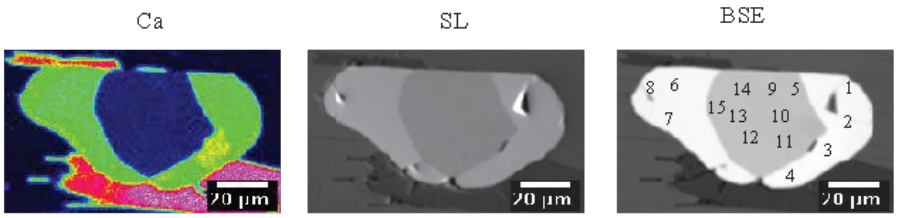

105
106
107

MA-11

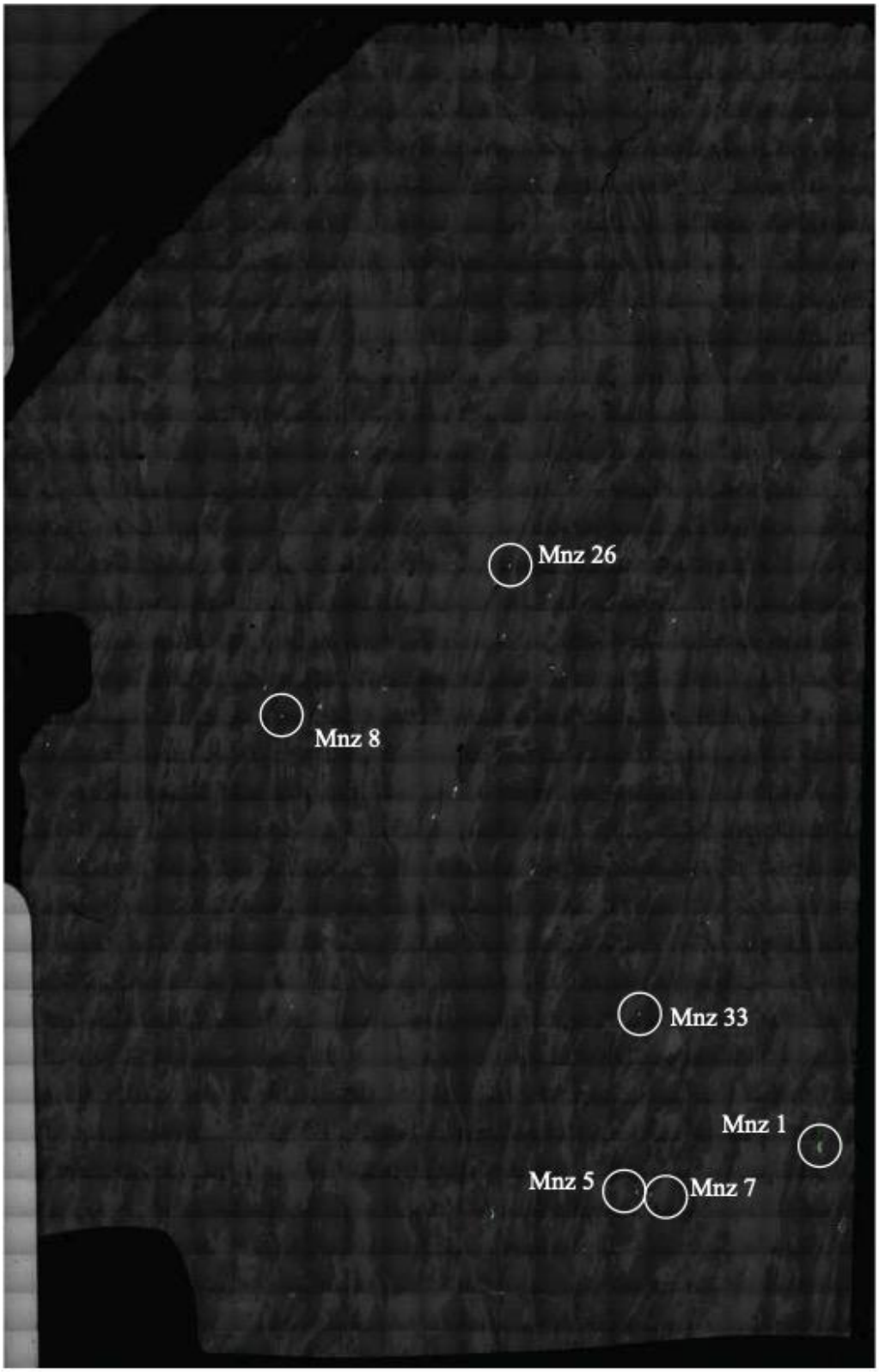

MA-11 mnz 1

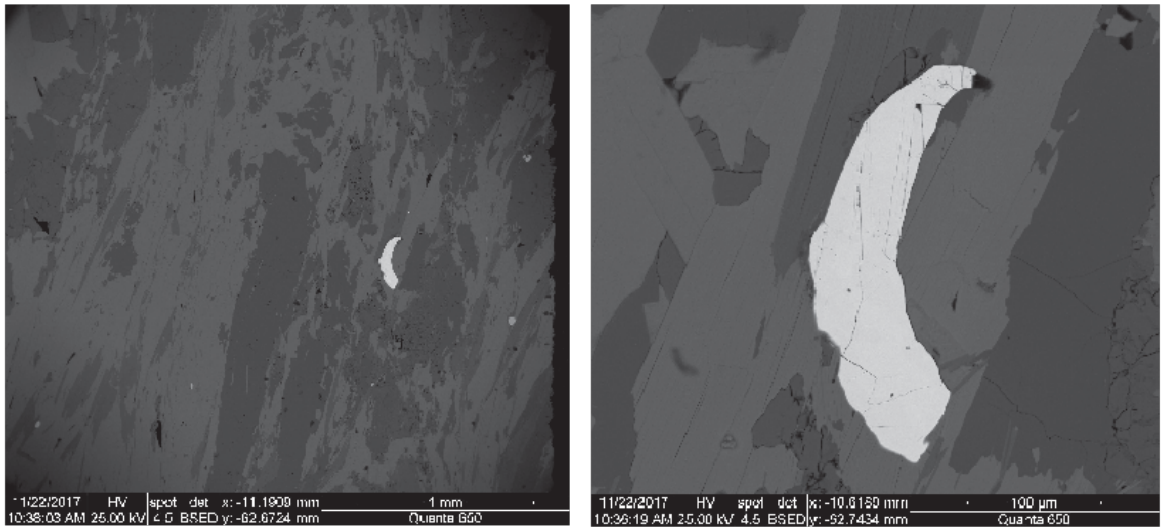

Y U Th Si

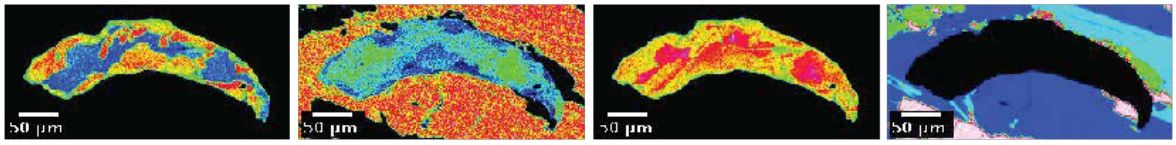

Ca SL BSE

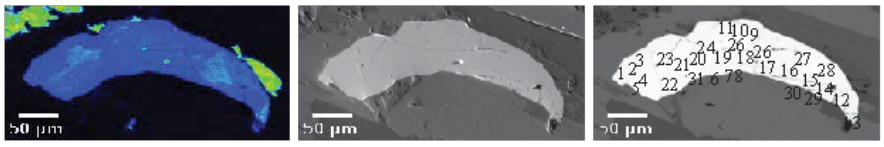

109
110
111

MA-11 mnz 5

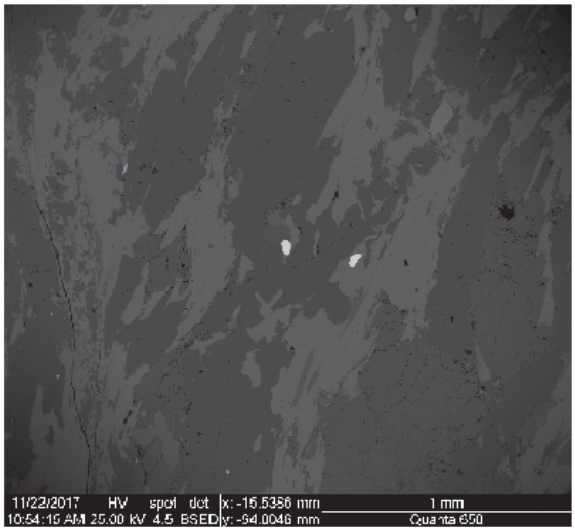

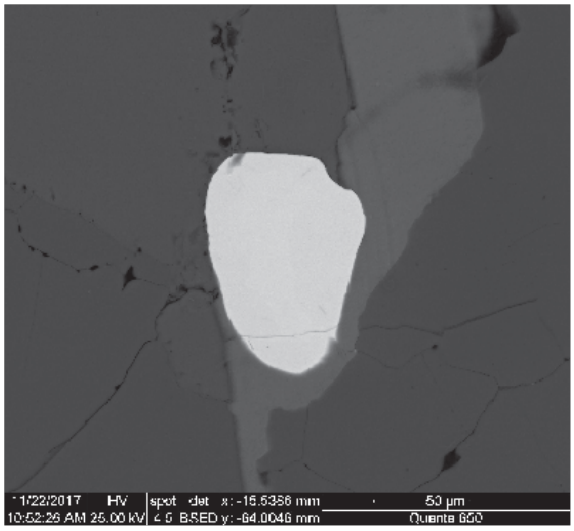

Y

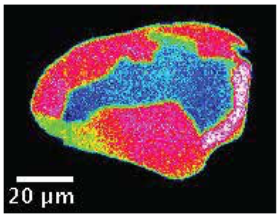

U

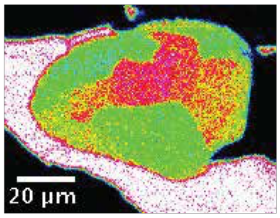

Th

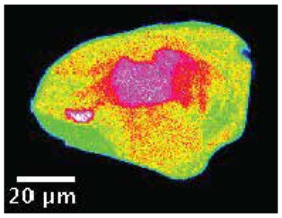

Si

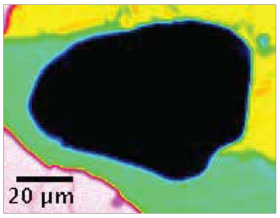

Ca

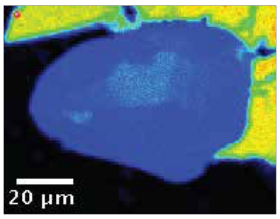

SL

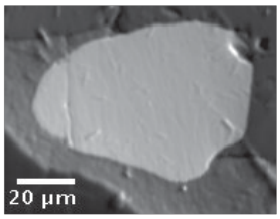

BSE

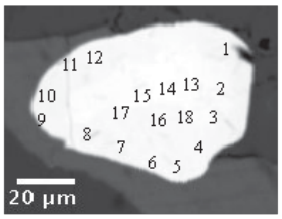

112
113
114

MA-11 mnz 7

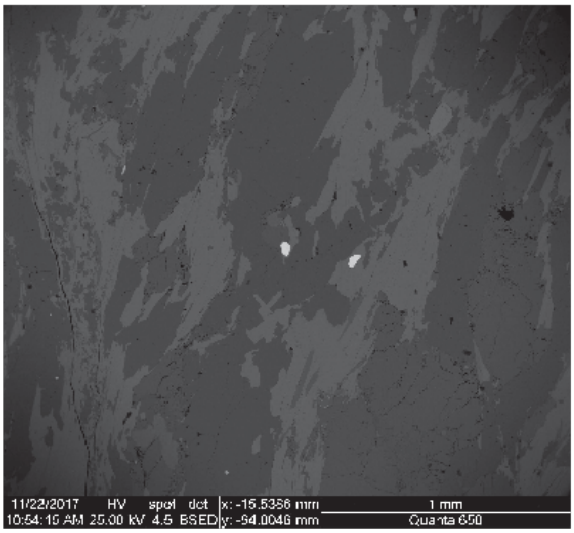

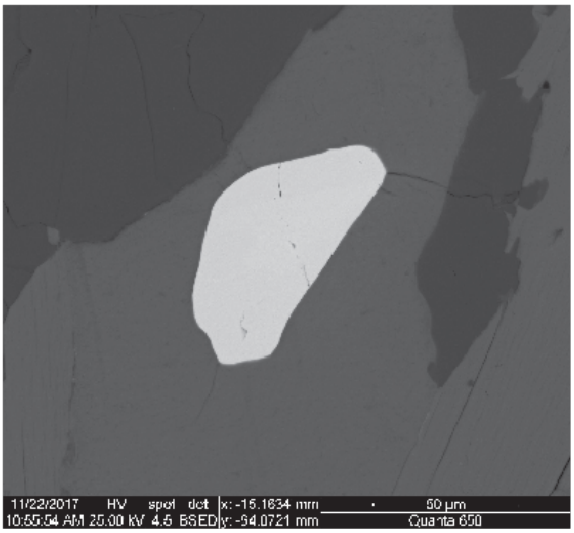

Y

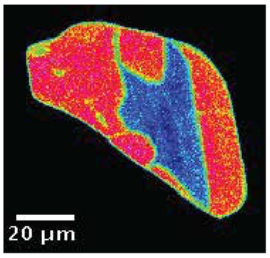

U

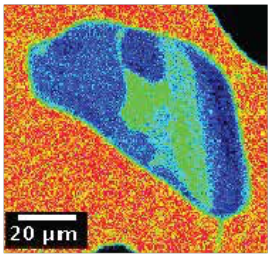

Th

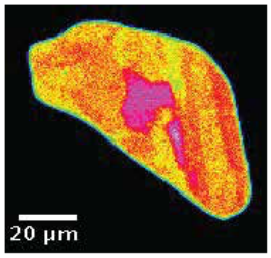

Si

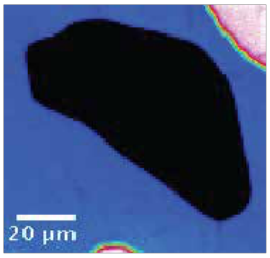

Ca

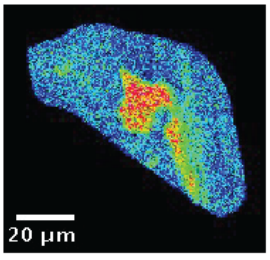

SL

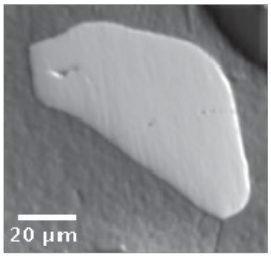

BSE

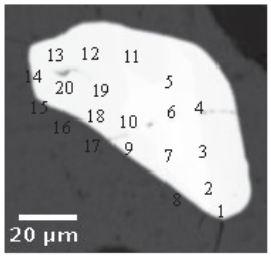

115
116
117

MA-11 mnz 8

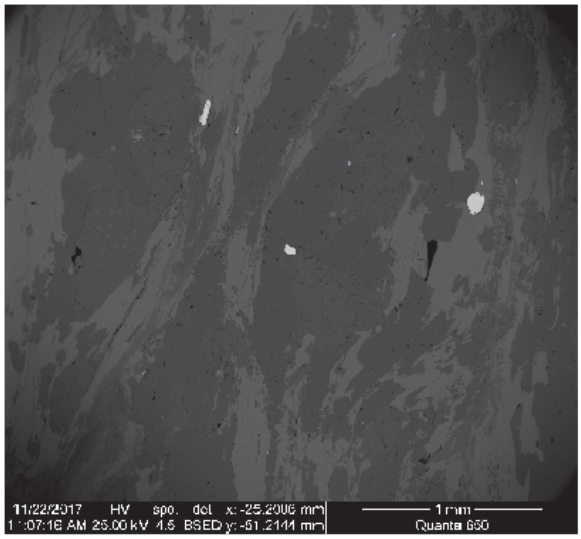

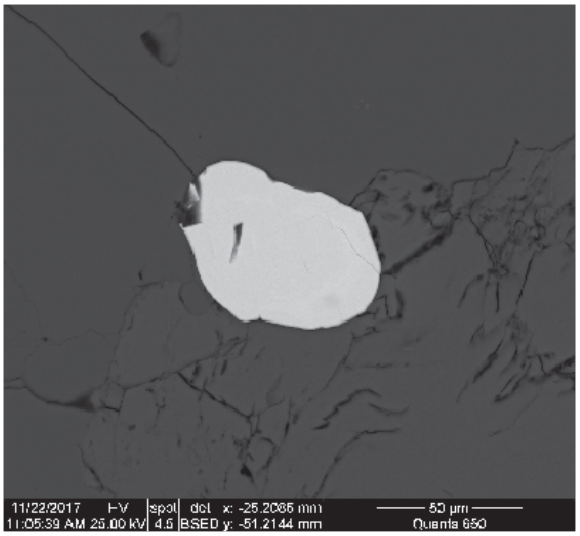

Y

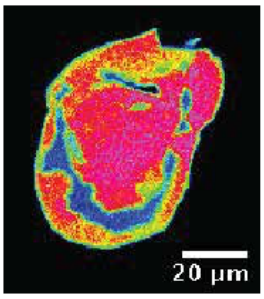

U

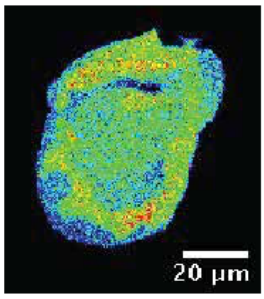

Th

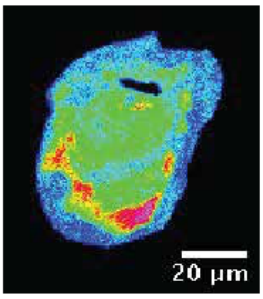

Si

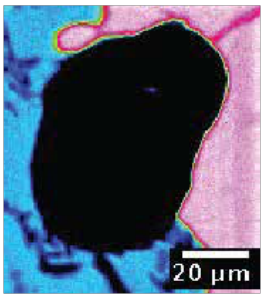

Ca

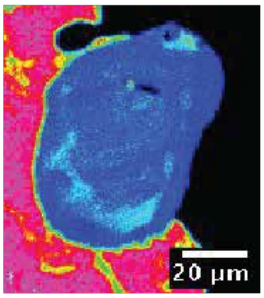

SL

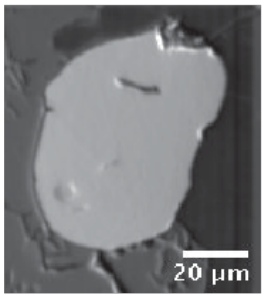

BSE

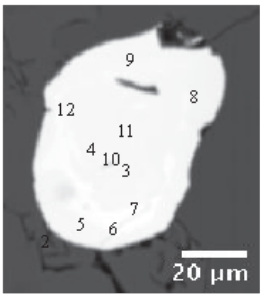

118
119
120

MA-11 mnz 26

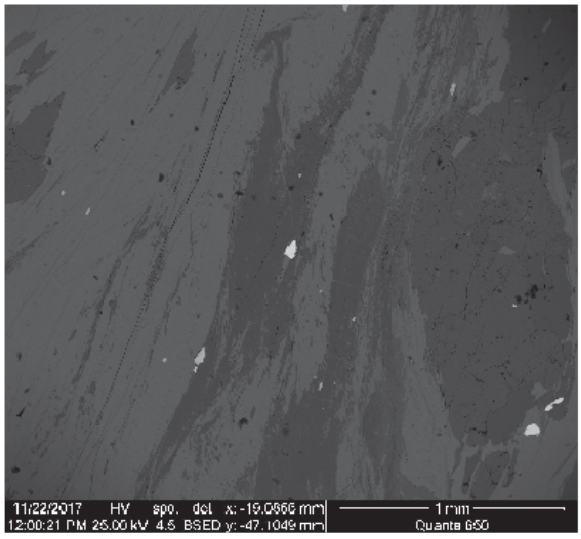

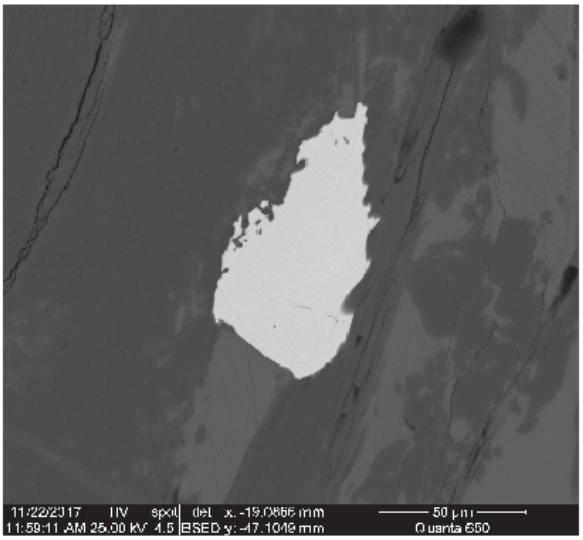

Y

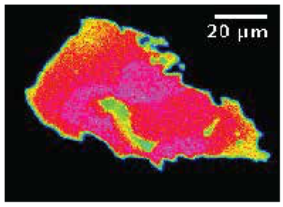

U

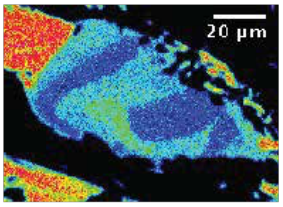

Th

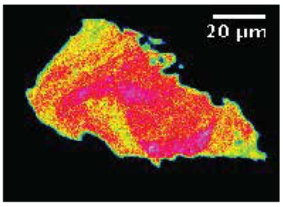

Si

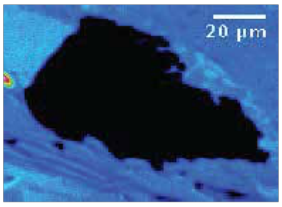

Ca

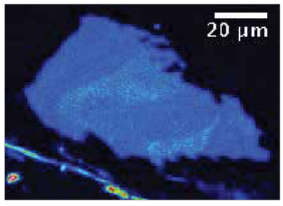

SL

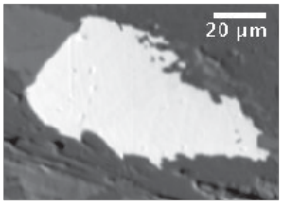

BSE

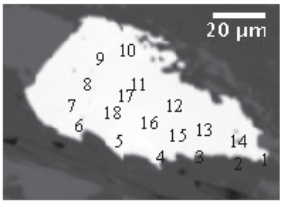

121
122
123

MA-11 mnz 33

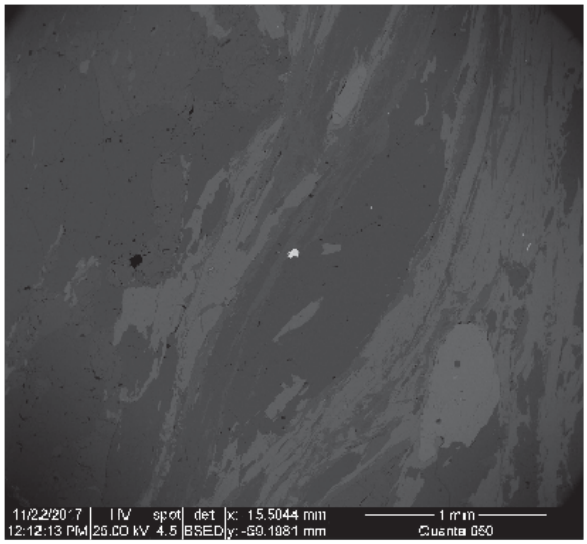

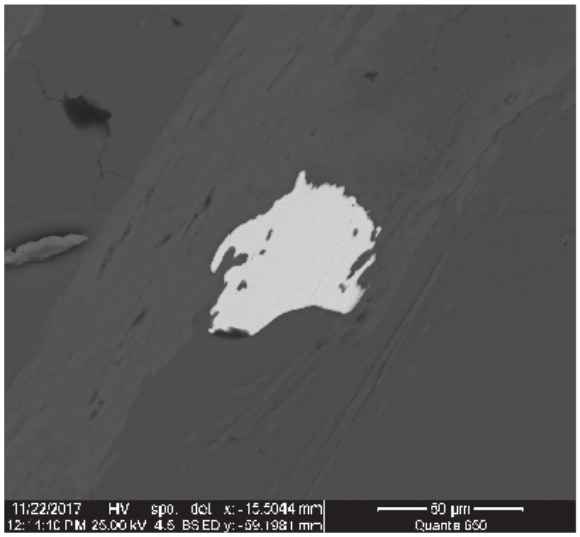

Y

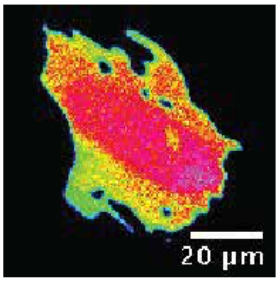

U

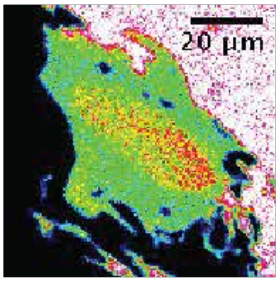

Th

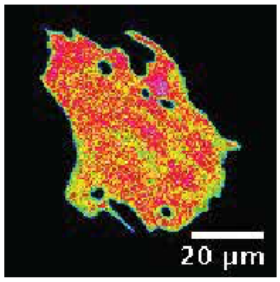

Si

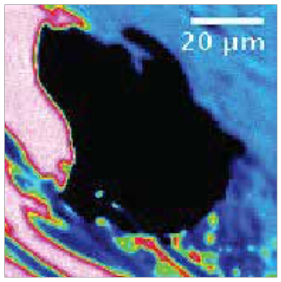

Ca

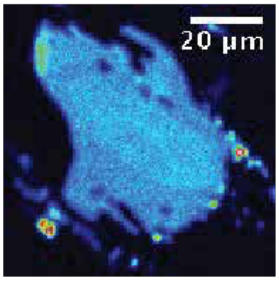

SL

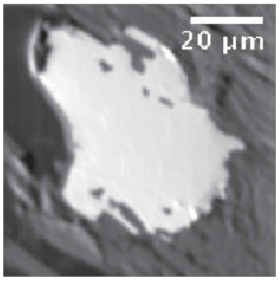

BSE

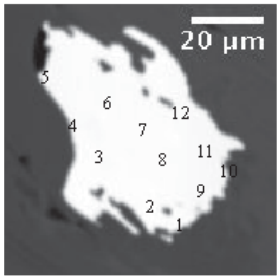

124
125
126

MA-21c

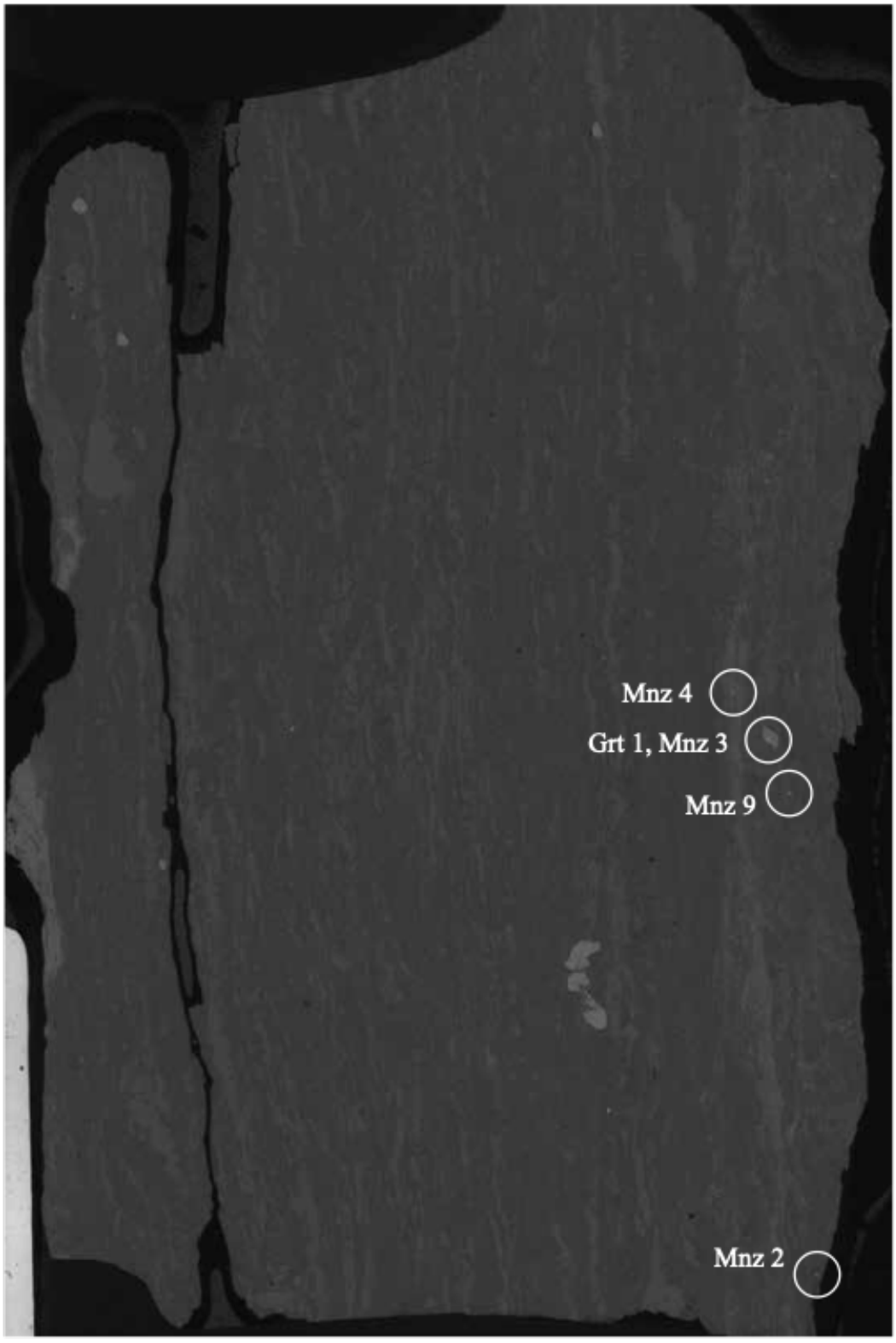

127

MA-21c mnz 2

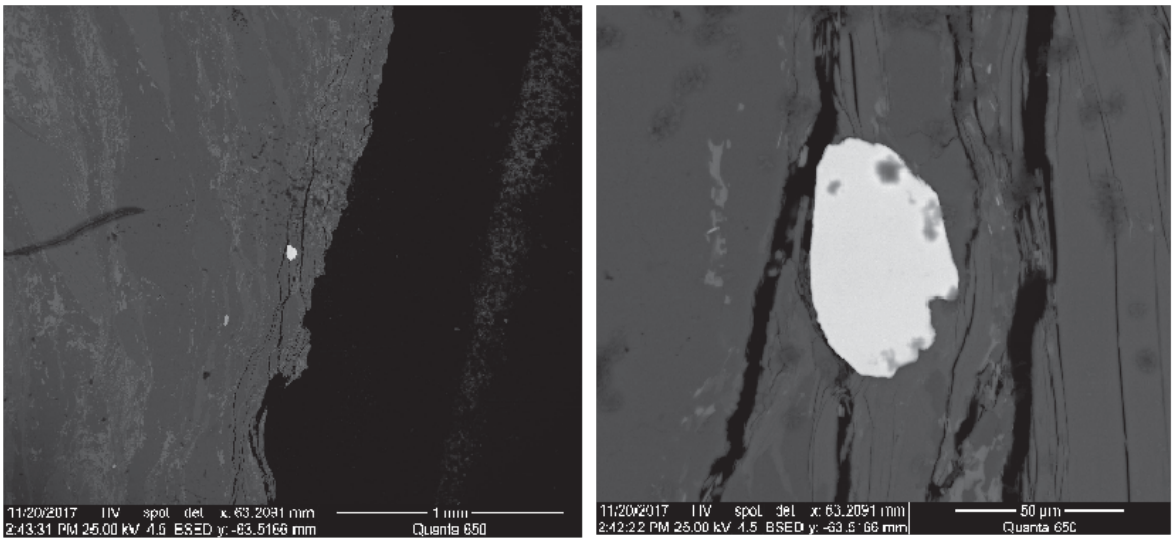

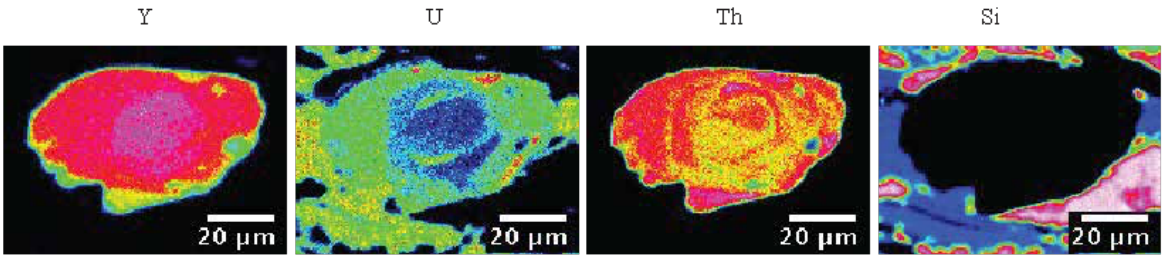

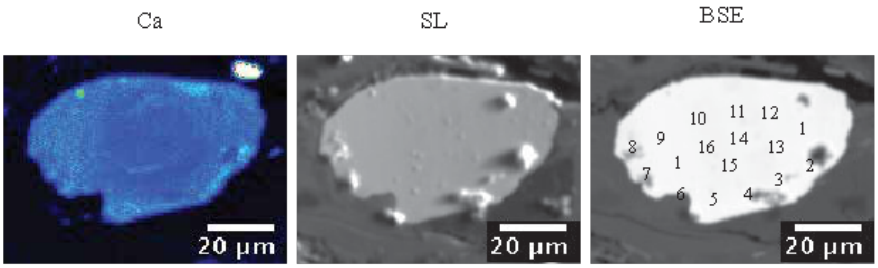

128
129
130

MA-21c mnz 3

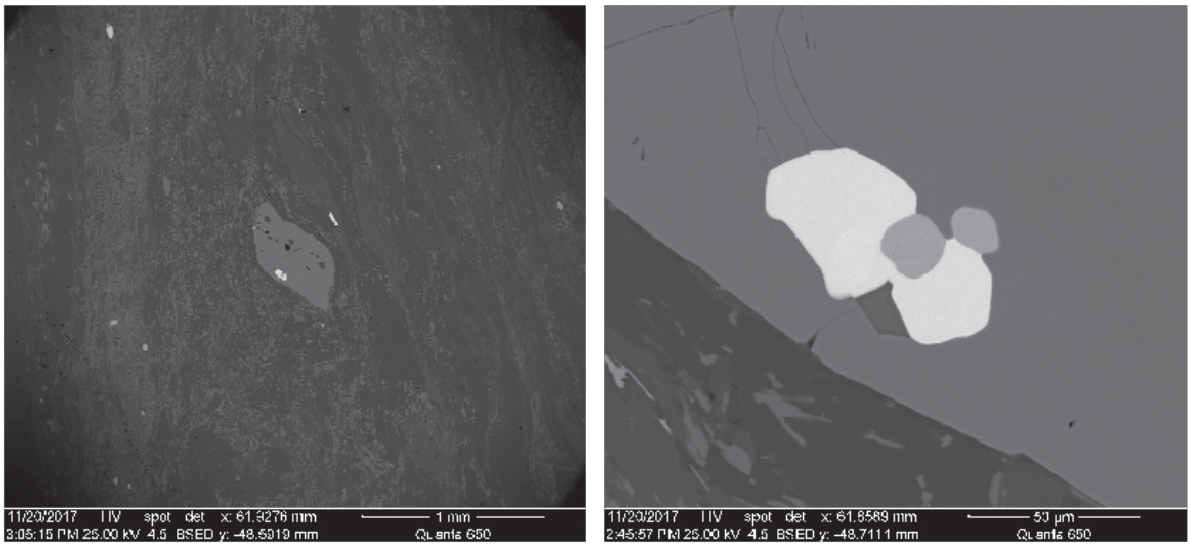

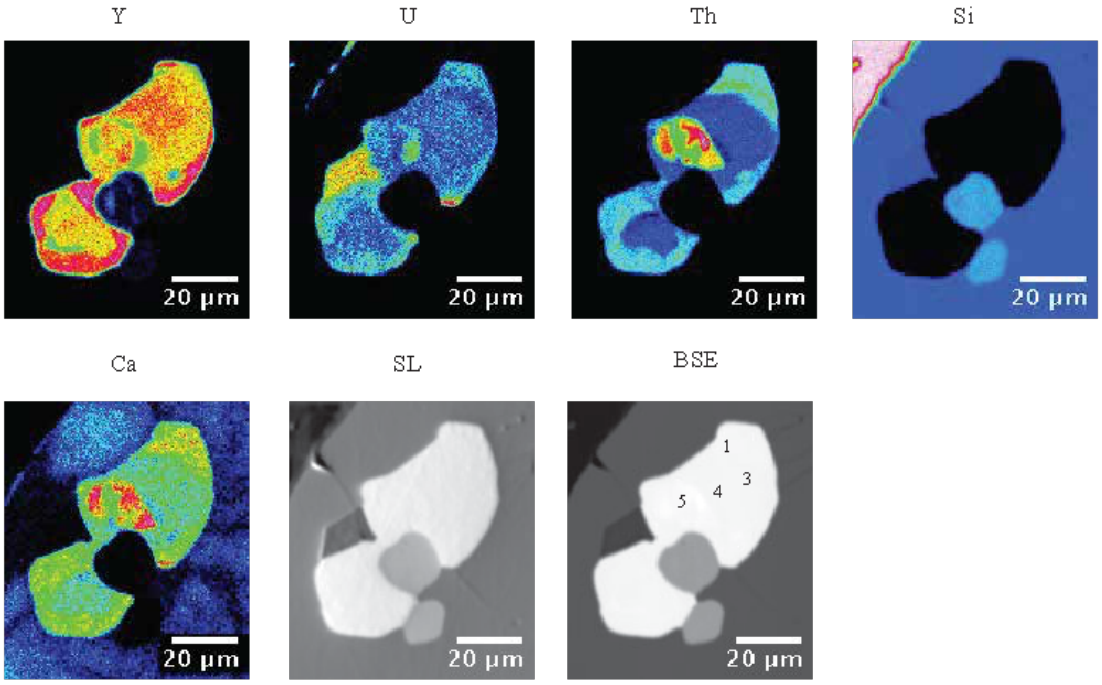

131
132
133

MA-21c mnz 4

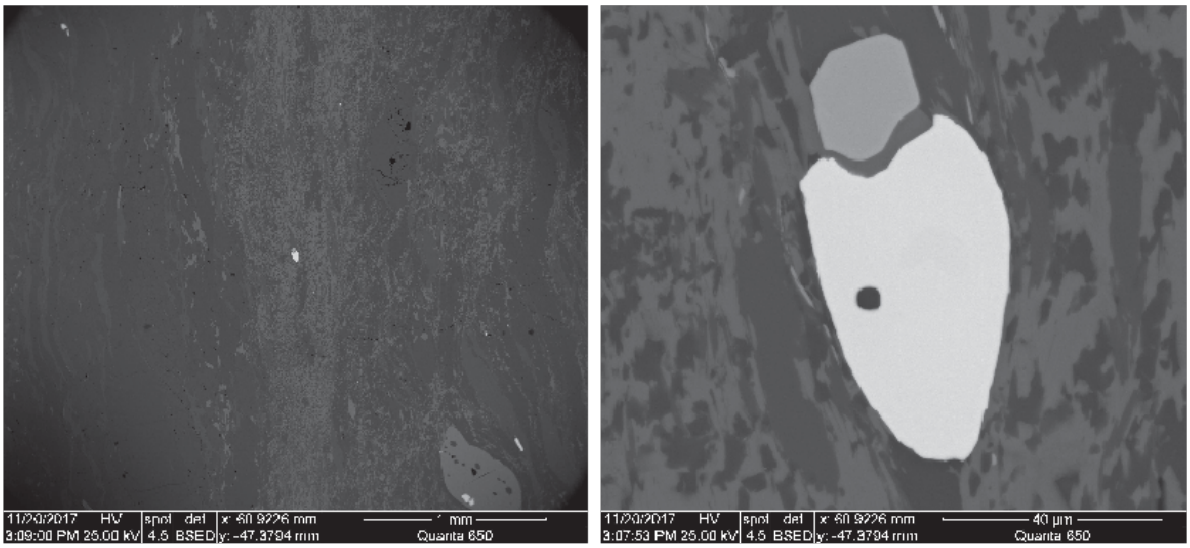

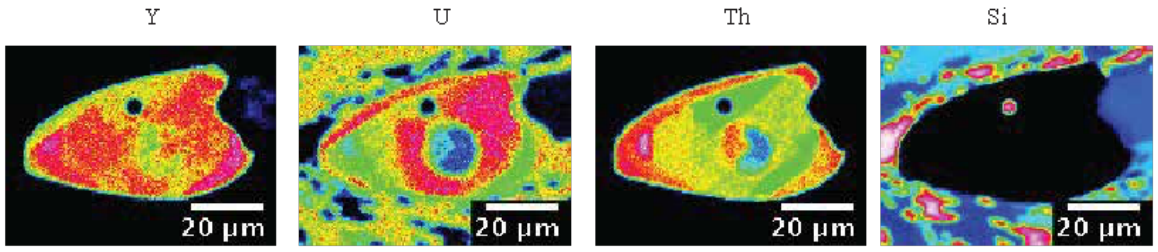

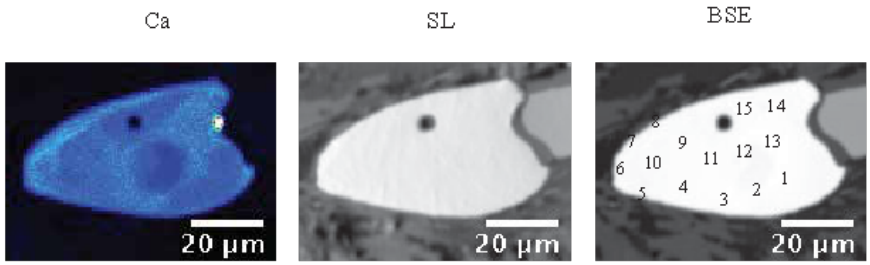

134
135
136

MA-21c mnz 9

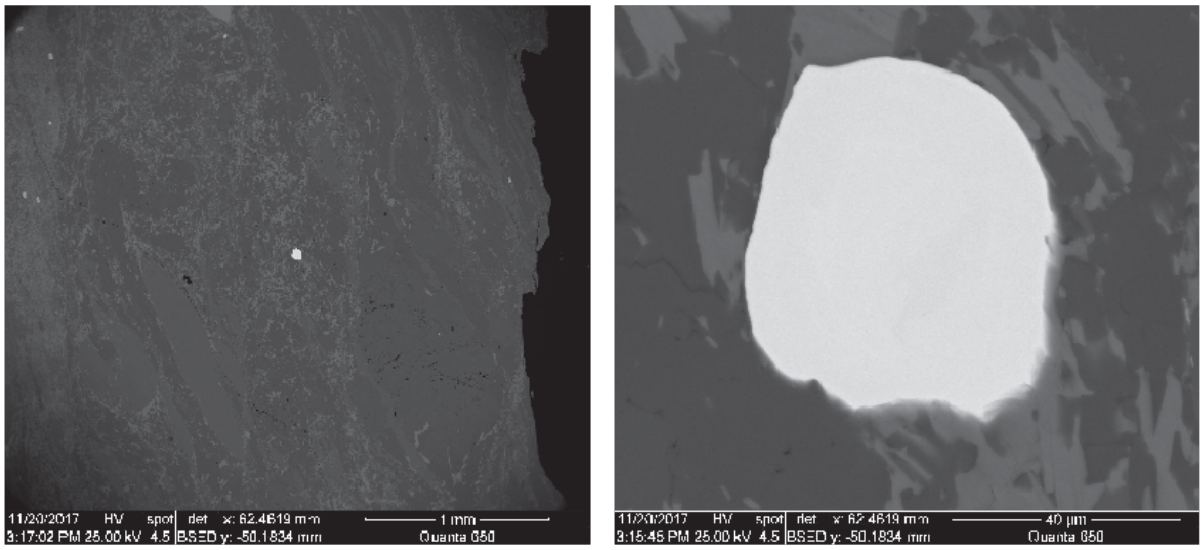

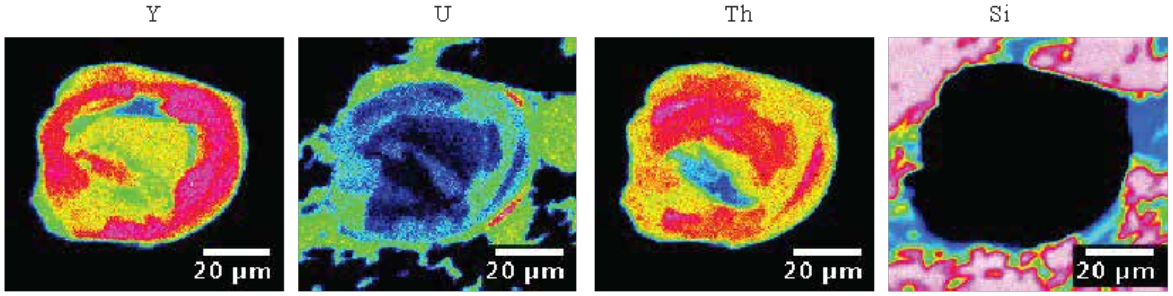

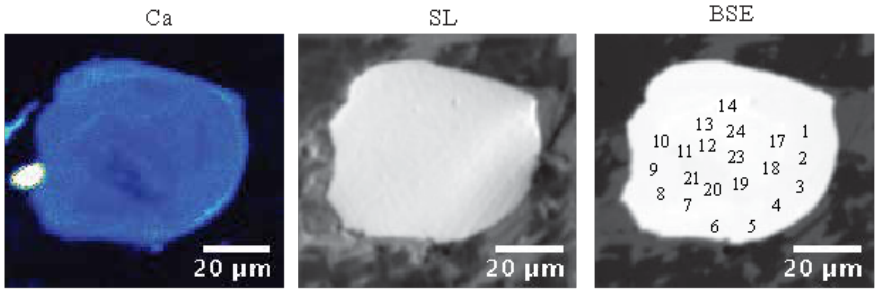

137
138
139

MA-26

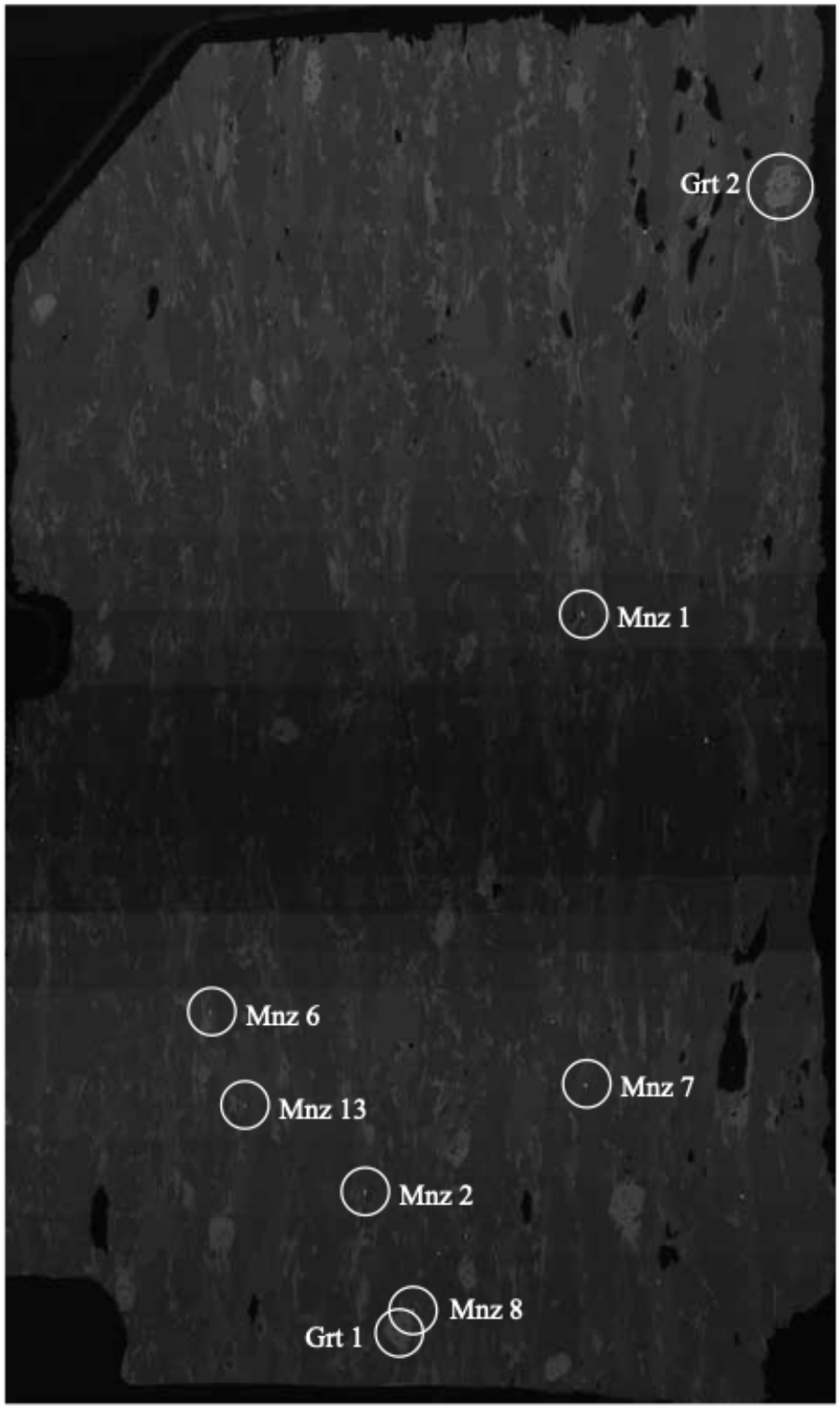

140

MA-26 mnz 1

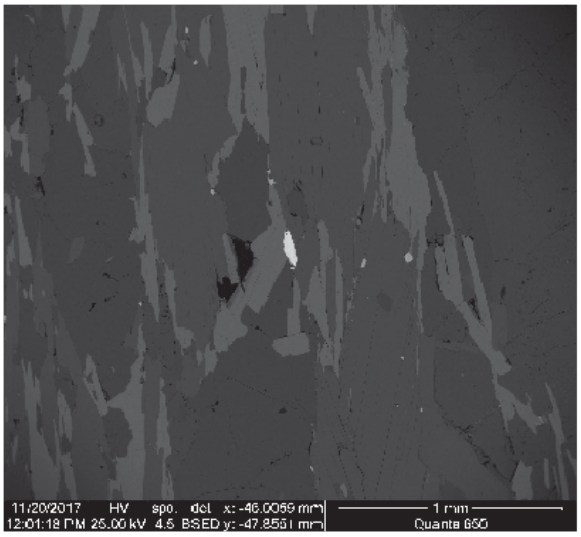

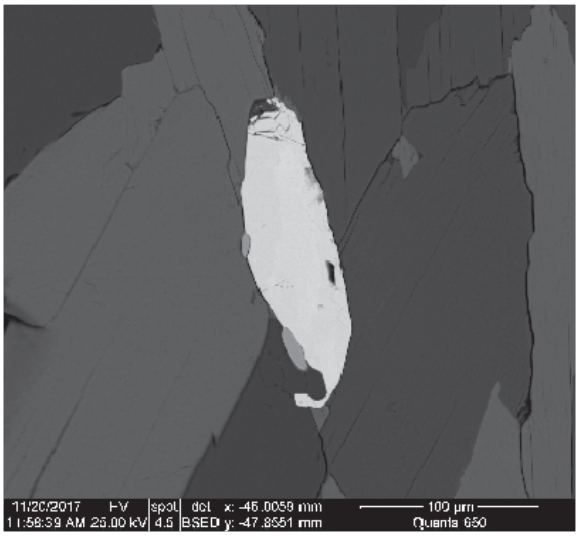

Y U Th Si

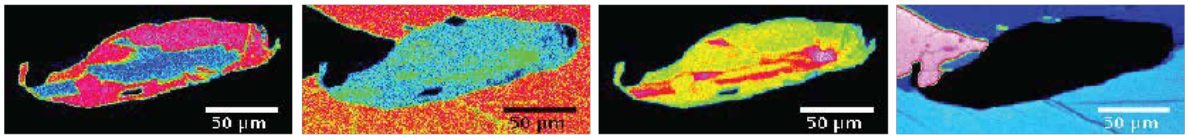

Ca SL BSE

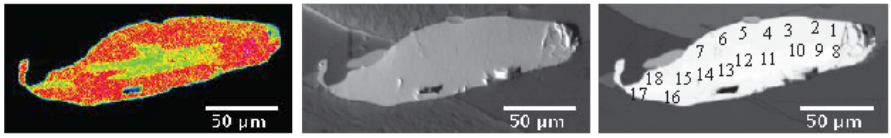

141
142
143

MA-26 mnz 2

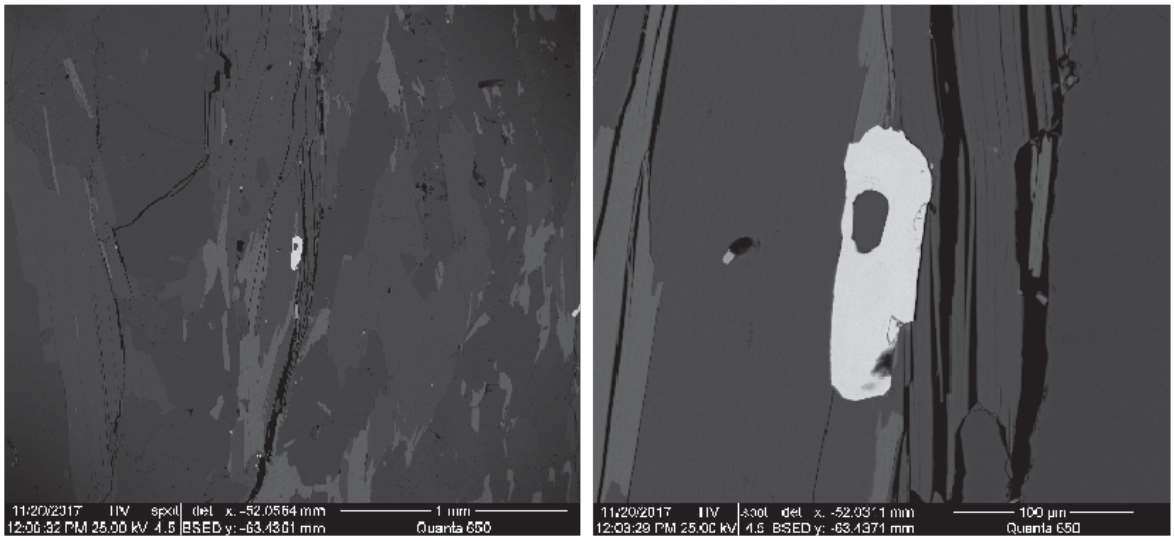

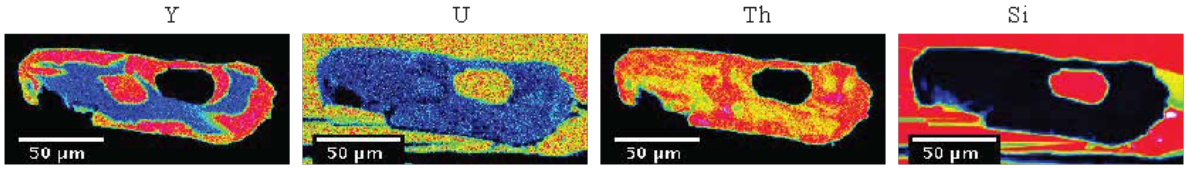

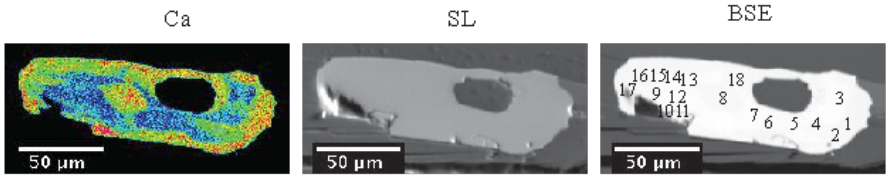

144
145
146

MA-26 mnz 6

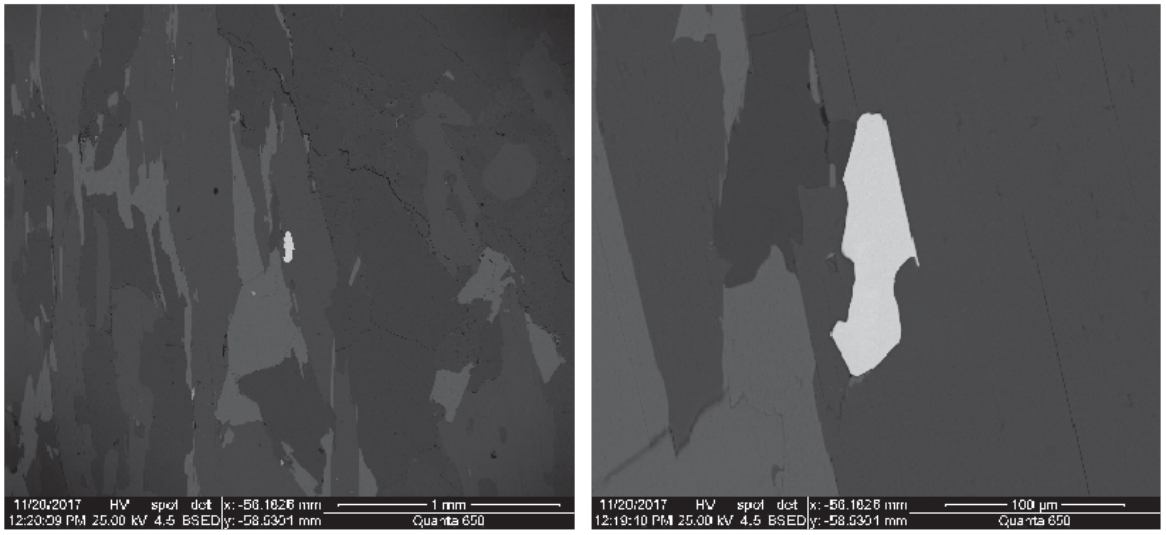

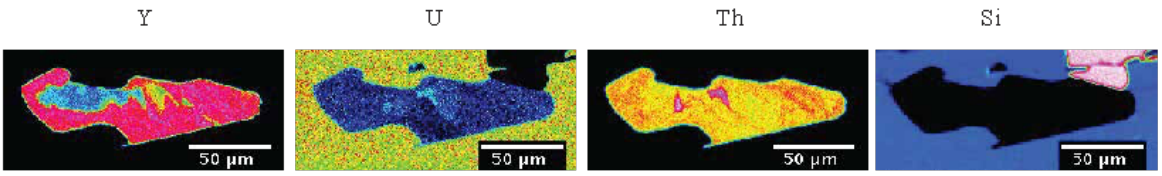

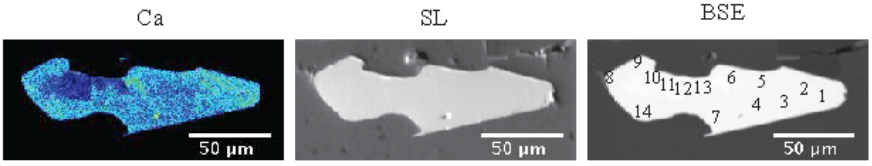

147
148
149

MA-26 mnz 7

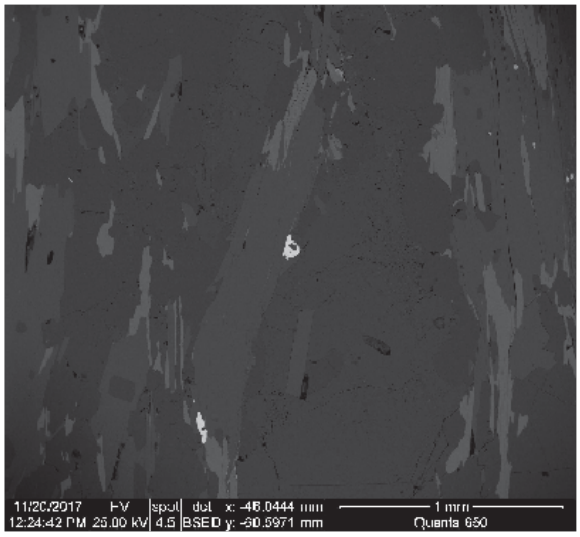

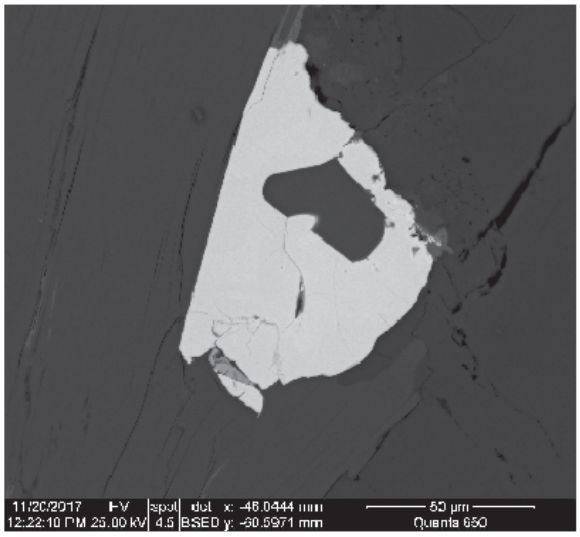

Y

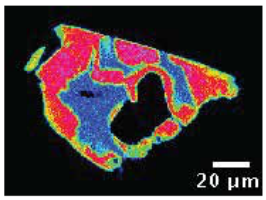

U

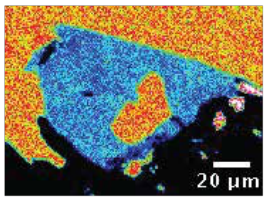

Th

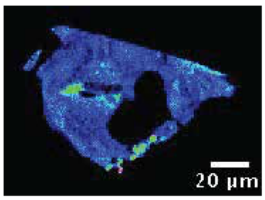

Si

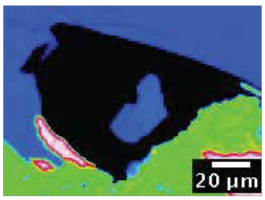

Ca

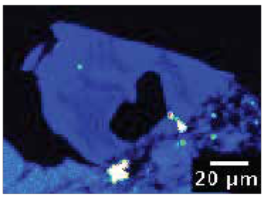

SL

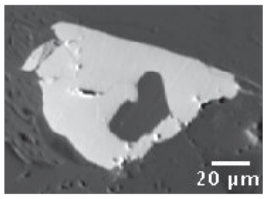

BSE

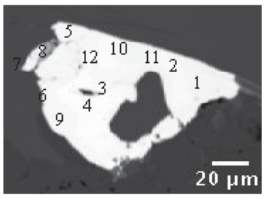

150
151
152

MA-26 mnz 8

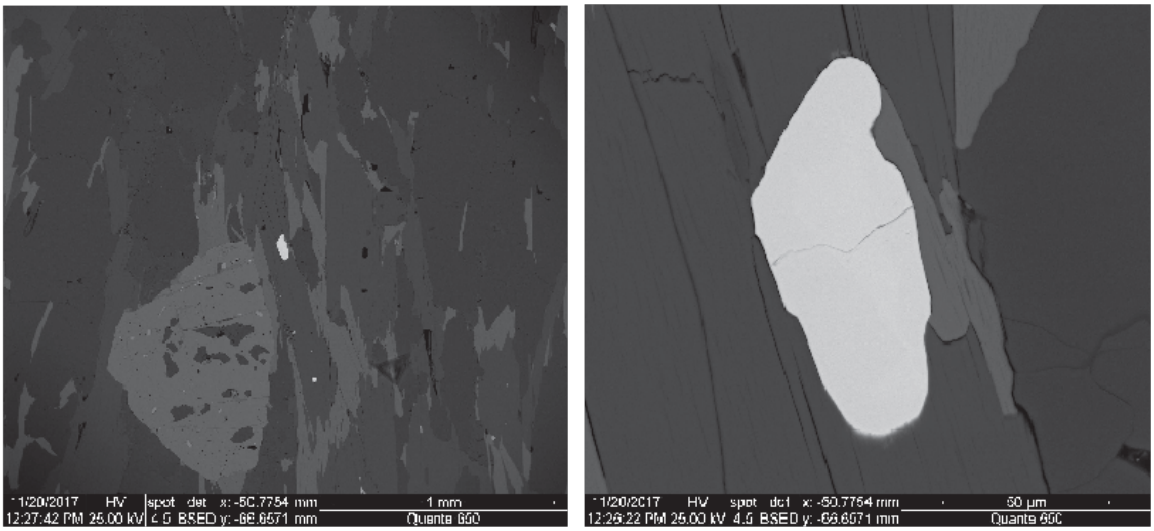

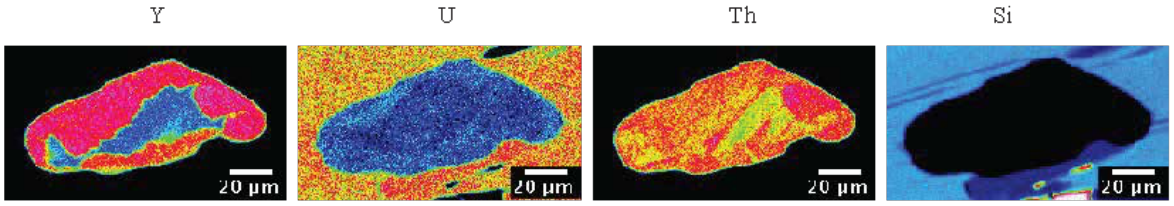

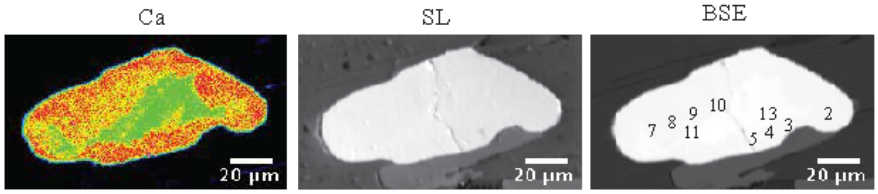

153
154
155

MA-26 mnz 13

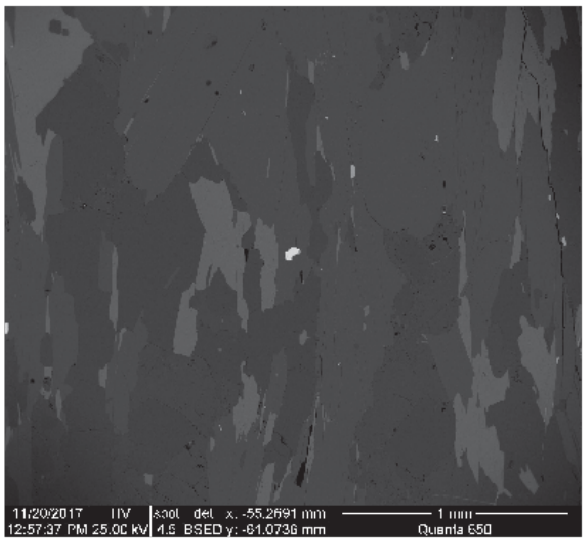

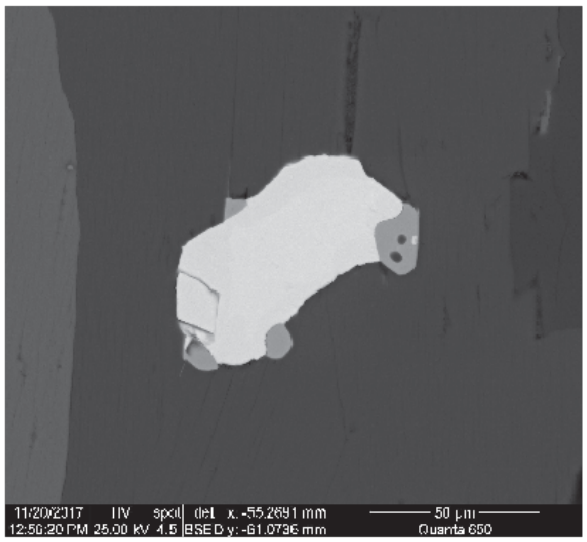

Y

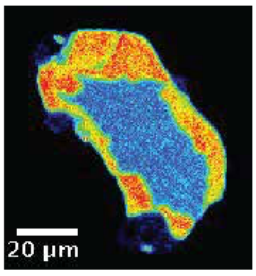

U

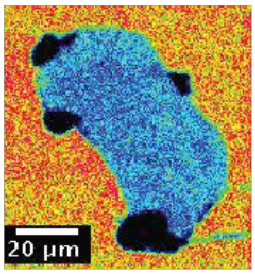

Th

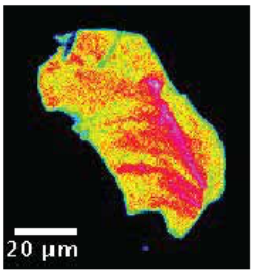

Si

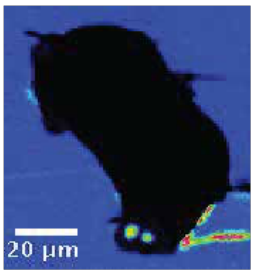

Ca

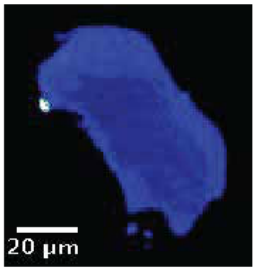

SL

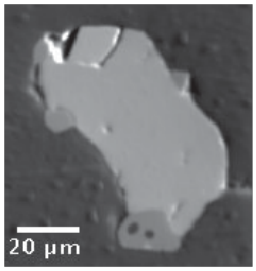

BSE

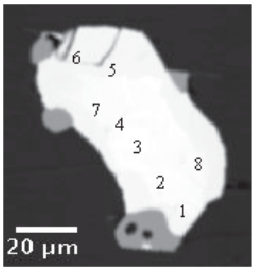

156
157
158

MA-21c grt 1

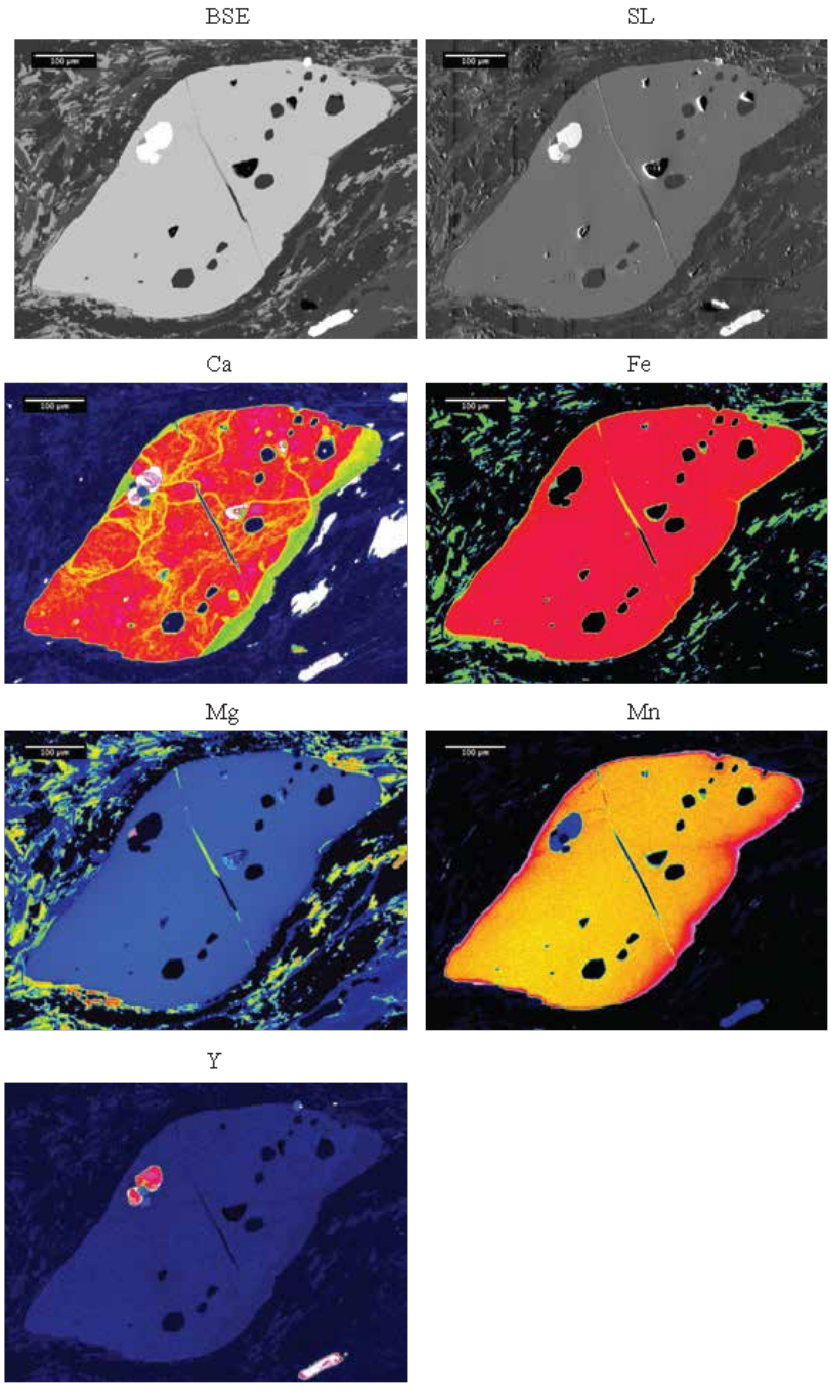

159
160
161

MA-26 grt 1

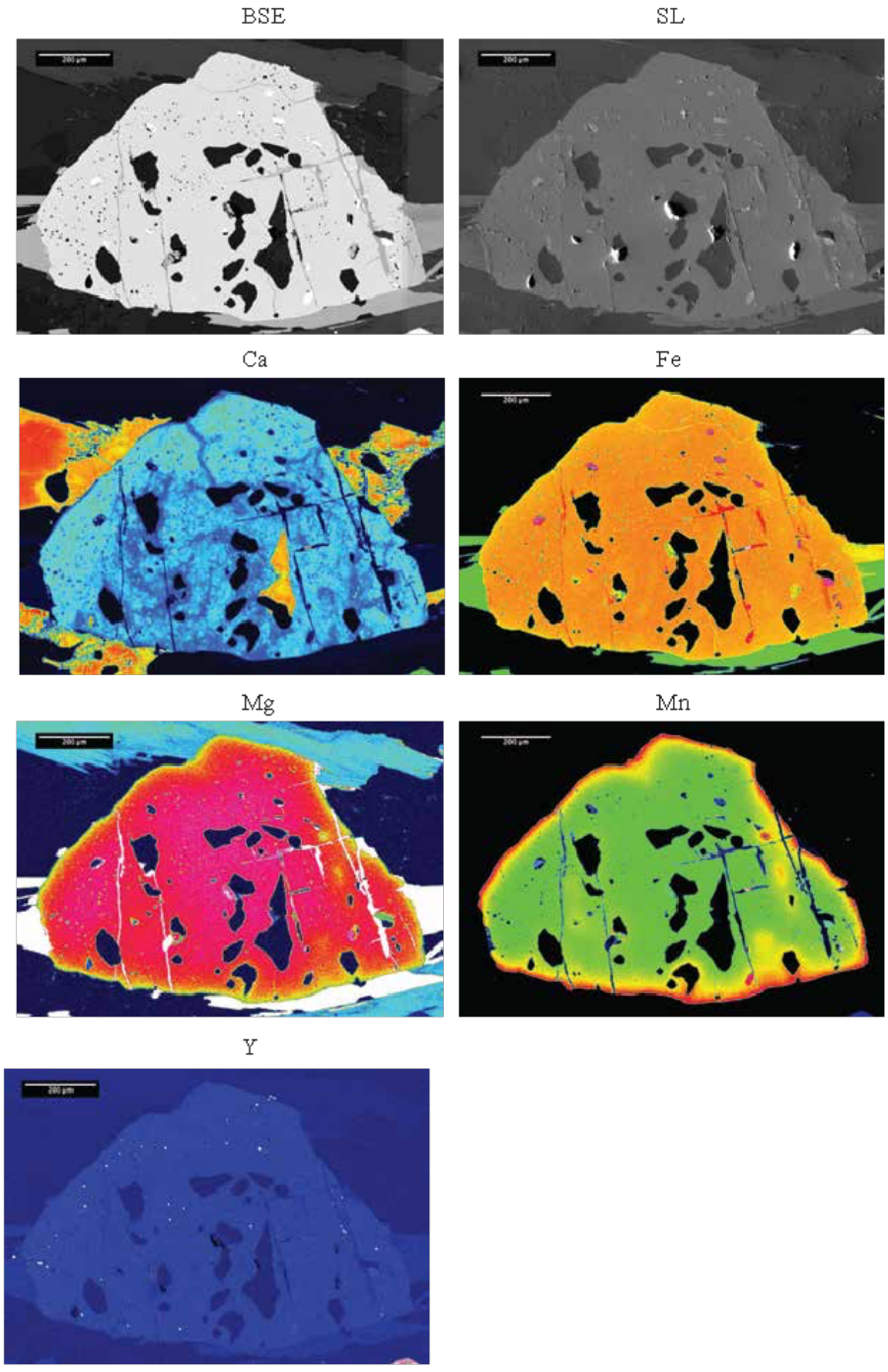

MA-26 grt 2

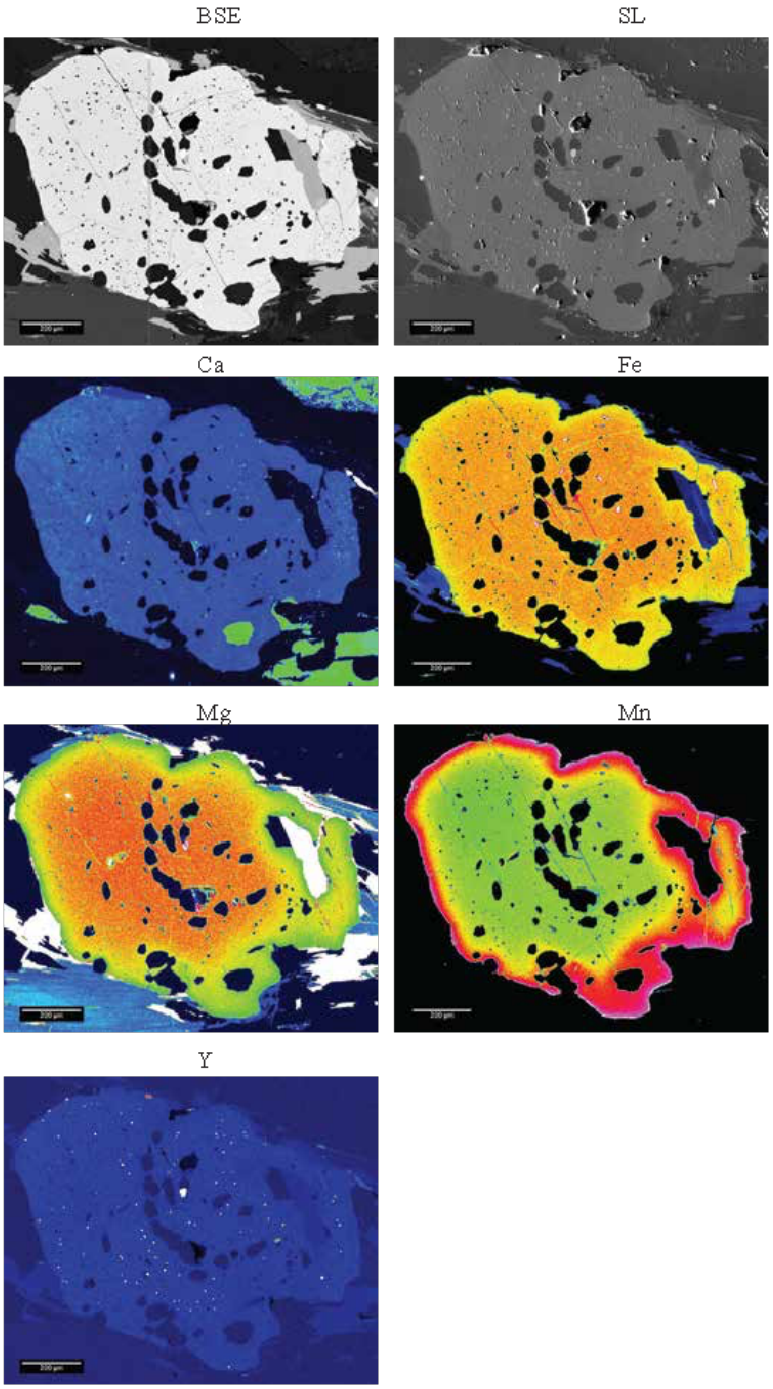

165
166

2C. U-Th/Pb monazite petrochronology data available in a separate Excel file

1D. References

Aleinikoff, J.N., Schenck, W.S., Plank, M.O., Srogi, L., Fanning, C.M., Kamo, S.L., and Bosbyshell, H., 2006, Deciphering igneous and metamorphic events in high-grade rocks of the Wilmington Complex, Delaware: Morphology, cathodoluminescence and backscattered electron zoning, and SHRIMP U-Pb geochronology of zircon and monazite: Geological Society of America Bulletin, v. 118(1-2), p. 39-64.

Amelin, Y. and Zaitsev, A.N., 2002' Precise geochronology of phosphorites and carbonatites: The critical role of U-series disequilibrium in age interpretations: Geochimica Cosmochimica Acta, v. 66, p. 2399–2419.

Goldstein, S., Onions, R., and Hamilton, P., 1984, A Sm-Nd isotopic study of atmospheric dustsand particulates from major river systems: Earth and Planetary Science Letters, v. 70, p. 221–236, doi: 10.1016/0012-821x(84)90007-4.

Horstwood, M.S.A., Foster, G.L., Parrish, R.R., Noble, S.R., Nowell, G.M., 2003, Common-Pb corrected in situ U-Pb accessory mineral geochronology by LA-MC-ICP-MS: Journal of Analytical Atomic Spectrometry, v. 18, p. 837–846, doi.org/10.1039/b304365g.

Jaffey, A.H., Flynn, K.F., Glendenin, L.E., Bentley, W.C., Essling, A.M., 1971, Precision measurement of the half-lives and specific activities of U235 and U238: Physical Reviews, C4, p. 1889–1906, doi.org/10.1103/PhysRevC.4.1889.

Kelsey, D.E., Clark, C., and Hand, M., 2008, Thermobarometric modelling of zircon and monazite growth in melt-bearing systems: examples using model metapelitic and metapsammitic granulites: Journal of Metamorphic Geology, v. 26, p. 199–212, doi: 10.1111/j.1525-1314.2007.00757.x.

Kohn, M.J., Wieland, M.S., Parkinson, C.D., and Upreti, B.N., 2005, Five generations of monazite in Langtang gneisses: implications for chronology of the Himalayan metamorphic core: Journal of Metamorphic Geology, v. 23, p. 399–406, doi: 10.1111/j.1525-1314.2005.00584.x.

Kylander-Clark, A.R., Hacker, B.R., and Cottle, J.M., 2013, Laser-ablation split-stream ICP petrochronology: Chemical Geology, v. 345, p. 99–112, doi: 10.1016/j.chemgeo.2013.02.019.

McKinney, S.T., Cottle, J.M., and Lederer, G.W., 2015, Evaluating rare earth element (REE) mineralization mechanisms in Proterozoic gneiss, Music Valley, California: Geological Society of America Bulletin, doi: 10.1130/b31165.1.

Paton, C., Woodhead, J.D., Hellstrom, J.C., Hergt, J.M., Greig, A., and Maas, R., 2010, Improved laser ablation U-Pb zircon geochronology through robust downhole fractionation correction: Geochemistry, Geophysics, Geosystems, v. 11, doi: 10.1029/2009gc002618.

Pyle, J.M., Spear, F.S., Rudnick, R.L, and McDonough, W.F., 2001, Monazite-Xenotime-Garnet Equilibrium in Metapelites and a New Monazite-Garnet Thermometer: Journal of Petrology, v. 42, p. 2083–2107, doi: 10.1093/petrology/42.11.2083.

Pyle, J.M., and Spear, F.S., 2003, Four generations of accessory-phase growth in low-pressure migmatites from SW New Hampshire: American Mineralogist, v. 88, p. 338–351, doi: 10.2138/am-2003-2-311.

Spear, F.S., and Pyle, J.M., 2002, Apatite, Monazite, and Xenotime in Metamorphic Rocks: Reviews in Mineralogy and Geochemistry, v. 48, p. 293–335, doi: 10.2138/rmg.2002.48.7.